

## Radion and Higgs mixing at the LHC

Masud Chaichian<sup>a,b</sup>, Anindya Datta<sup>c</sup>, Katri Huitu<sup>a</sup> and Zenghui Yu<sup>a,b</sup>

<sup>a</sup>Helsinki Institute of Physics

<sup>b</sup>Department of Physics, University of Helsinki  
P.O.Box 9, FIN-00014 Helsinki, Finland

<sup>c</sup>Harish-Chandra Research Institute  
Chhatnag Road, Jhusi, Allahabad-211 019, India

### ABSTRACT

We study the resonance production of radions and Higgs via gluon-gluon fusion in the Randall-Sundrum model with Higgs-curvature mixing at the LHC. We find that radion can be detected both in mixed (with Higgs boson) and unmixed case if the radion vacuum expectation value  $\Lambda_\phi$  is around 1 TeV. The  $\Lambda_\phi \sim 10$  TeV case is also promising for certain values of mixing parameters and radion masses. The mixing can affect the production and decay of Higgs boson in a significant way. Thus Higgs search strategies at the LHC may need refinements in case of radion-Higgs mixing in the Randall-Sundrum model.

## I. Introduction

Recently proposed scenarios involving extra dimensions [1, 2] provide an interesting possibility to probe the structure of the space-time at TeV colliders. These models try to relate two fundamental scales of physics, namely the Planck scale and the electroweak scale. All these models assume our world is  $(4+n)+1$  dimensional, where the extra  $n$  space-like dimensions are curled up with compactification radius smaller than the current experimental reach. The ADD [1] model requires relatively large compactification radius ( $\sim 1$  mm). In the following we will be interested in the phenomenology of the model by Randall and Sundrum (RS) [2]. RS model assumes our universe is  $(4+1)$  dimensional. Unlike the ADD, this scenario does not require a large compactification radius for this extra compactified space-like dimension. Moreover in RS model the radius of compactification is of the order of Planck length and interestingly is a dynamical object. It is connected to the vacuum expectation value of the dilaton field arising due to compactification of full 5 dimensional theory to 4 dimensions. Radion field is basically the exponential of this dilaton field scaled by proper factors. Goldberger and Wise have shown [3, 4] that one can write a potential for this radion field by adding a scalar field to the bulk and dynamically generate the VEV. It was also shown that without doing any fine tuning to the parameters of the theory, this VEV can be of the order of TeV. Radion mass in the stabilised RS model comes out to be typically lighter than the low-lying Kaluza-Klein modes of graviton [3, 5]. Thus radion might be the first state, which is specific to the model and accessible to the next generation TeV colliders.

The phenomenology of radions has been discussed in several works [5, 6, 7, 8, 9, 10]. We will concentrate on the aspects of Higgs-curvature mixing [11, 12] in this paper. Mixing is due to the following term in the action.

$$S = -\xi \int d^4x \sqrt{-g_{vis}} R(g_{vis}) H^\dagger H, \quad (1.1)$$

The Ricci scalar  $R(g_{vis})$  corresponds to the induced four dimensional metric,  $g_{vis}$ , on the visible brane and  $H$  is the electroweak Higgs boson. This term will introduce mixing between radion and Higgs in the RS model. Since the Higgs search is one of the main goals of the future collider experiments, the mixing of Higgs with another particle is of major importance, if it will change the Higgs production or decay patterns. We will see in the following that mixing of radion with Higgs will modify the Higgs and radion phenomenology significantly.

The radion production via gluon-gluon fusion dominates the production process of radion at LHC [7], and the effects of radion for  $Z$  boson pair production have already been considered in [10]. The effects of the Higgs-curvature mixing on radion production at LC were also considered

in [13]. In the present paper we will discuss the resonance production of radion and Higgs via gluon-gluon fusion ( $pp (gg) \rightarrow h', \phi'$ ), which may probe a wide mass range making it possible to study the effects of curvature-Higgs mixing at the LHC.<sup>1</sup>

In section 2, we will discuss the coupling of radion and Higgs to the Standard Model (SM) fields, and in section 3 we discuss the decay modes of Higgs and radion in the case of the curvature-Higgs mixing. Section 3 will also contain the numerical results of radion and Higgs production. We conclude in section 4. Some details of the expressions are listed in the Appendix.

## II. Curvature-Higgs mixing in the Randall-Sundrum model.

The action (1.1) leads to the curvature-Higgs mixing Lagrangian [11, 12] given by

$$\mathcal{L} = -6\xi\Omega^2 \left( \square \ln \Omega + (\nabla \ln \Omega)^2 \right) H^\dagger H, \quad (2.1)$$

where

$$\Omega = e^{-(\gamma/v)\phi(x)}, \quad \gamma = v/\Lambda_\phi.$$

Here  $v$  is the Higgs VEV and  $\Lambda_\phi$  is the radion VEV.

The interactions in (2.1) will induce the curvature-Higgs mixing, as discussed in the Appendix. The couplings of the physical radion and Higgs ( $\phi', h'$ ) to the SM gauge fields and fermions will be modified to

$$\mathcal{L} = -\frac{1}{\Lambda_\phi} (m_{ij} \bar{\psi}_i \psi_j - M_V^2 V_{A\mu} V_A^\mu) \left[ a_{34} \frac{\Lambda_\phi}{v} h' + a_{12} \phi' \right], \quad (2.2)$$

where  $a_{12} = a + c/\gamma$  and  $a_{34} = d + b\gamma$ , where  $a, b, c, d$  are the mixing parameters given in the Appendix. It is seen that the mixing changes significantly the couplings of Higgs and radion to the SM fields. For example, as pointed out in Ref. [11],  $a_{12}$  can be approximately zero in the conformal limit  $m_h = 0, \xi = 1/6$  when  $\Lambda_\phi \gg v$ .

The coupling of the radion to two Higgs bosons depends on the scalar potential,  $V(\phi)$  and mixing of radion and Higgs. Neglecting the radion self-coupling in  $V(\phi)$ , we can get the vertex of  $h' h' \phi'$  as

$$V_{\phi' h' h'} = \frac{1}{\Lambda_\phi} \left( 2m_h^2 a d^2 h'^2 \phi' - a d^2 \phi' \partial_\mu h' \partial^\mu h' (1 - 6\xi) + 6\xi a d^2 (h' \square h') \phi' + 4m_h^2 b c d \phi' h'^2 - 2b c d h' \partial_\mu \phi' \partial^\mu h' (1 - 6\xi) + 6b c d \xi h' (\phi' \square h' + h' \square \phi') \right). \quad (2.3)$$

Trace anomaly significantly modifies the radion and Higgs coupling to  $gg$  and  $\gamma\gamma$  [17]. The effective vertices are given by

$$V_{gg} = \left[ \frac{1}{\Lambda_\phi} (a b_3 - \frac{1}{2} a_{12} F_{1/2}(\tau_t)) \phi' + \frac{1}{v} \left( \frac{v}{\Lambda_\phi} b b_3 - 1/2 a_{34} F_{1/2}(\tau_t) \right) h' \right] \frac{\alpha_s}{8\pi} G_{\mu\nu}^a G^{\mu\nu a} \quad (2.4)$$

<sup>1</sup>The states  $h'$  and  $\phi'$  are the physical ones after the mixing.

for radion and Higgs to gluons and

$$V_{\gamma\gamma} = \left[ \frac{1}{\Lambda_\phi} \{a(b_2 + b_Y) - a_{12}(F_1(\tau_W) + \frac{4}{3}F_{1/2}(\tau_t))\} \phi' + \frac{1}{v} \{ \frac{v}{\Lambda_\phi} b(b_2 + b_Y) - a_{34}(F_1(\tau_W) + \frac{4}{3}F_{1/2}(\tau_t)) \} h' \right] \frac{\alpha_{EM}}{8\pi} F_{\mu\nu} F^{\mu\nu} \quad (2.5)$$

for radion or Higgs coupling to a pair of photons, where  $b_3 = 7$  is the QCD  $\beta$ -function coefficient and  $b_2 = 19/6, b_Y = -41/6$  are the  $SU(2) \times U(1)_Y$   $\beta$ -function coefficients in the SM.  $F_1$  and  $F_{1/2}$  are form factor from loop effects, which will be given in detail in the Appendix. In each of these couplings the first term proportional to  $b_3$  or  $b_2 + b_Y$  are coming from the trace anomaly. The rest are from the electroweak symmetry breaking. We can see from Eq.(2.4,5) that the vertices Higgs-gluon-gluon and Higgs-photon-photon have new contributions, which change the production and decay of the Higgs boson.

As seen in the Appendix, the mixing matrix of radion and Higgs is not unitary. Therefore it is not always straightforward, which particle should be called Higgs and which should be called radion. We will always call  $\phi'$  radion and  $h'$  Higgs in the following calculations.

### III. Radion and Higgs production and decay

The experimental groups at LHC have made thorough studies of the possibilities to observe the Standard Model Higgs bosons at LHC. The most straightforward detection modes, with the corresponding Higgs mass ranges are (see e.g. [14])

$$\begin{aligned} H \rightarrow \gamma\gamma, & \quad 100 \text{ GeV} < m_H < 150 \text{ GeV}, \\ H \rightarrow WW, & \quad 150 \text{ GeV} < m_H < 190 \text{ GeV}, \\ H \rightarrow ZZ, & \quad 190 \text{ GeV} < m_H < \sim 700 \text{ GeV}. \end{aligned} \quad (3.1)$$

These are the decay modes of Higgs and radion that we will study in this work.

Because of the mixing the decay patterns of Higgs and radion will change. In Figure 1 we present the decay branching ratios of Higgs and radion in the mixed case, with the mixing parameter  $\xi = 1/6$ ,  $\Lambda_\Phi = 1 \text{ TeV}$ , and  $m_h = 150 \text{ GeV}$ . From Fig. 1 it is evident that when  $h'$  is heavier than 180 GeV the decay of Higgs to WW and ZZ will dominate. For radions heavier than twice the physical Higgs mass, the decay to Higgs and for larger masses to gluons will be dominant. If the radion VEV is increased, the branching ratios do not change significantly. Compared to the unmixed case, the branching ratios of heavy radion are changed. In the unmixed case, also for heavy radion, the dominant decay modes are the weak gauge bosons, and the branching ratio to gluons is at the percentage level [7, 13]. There are few other interesting points which we want to point out. The  $h'$  branching ratio to gluons has a sharp dip around  $m_{h'} = 250 \text{ GeV}$ . This can be explained by the structure of the  $h'gg$  coupling. This coupling has two terms. Second term is complex when  $h'$  mass is greater than  $2m_t$ . (The imaginary part

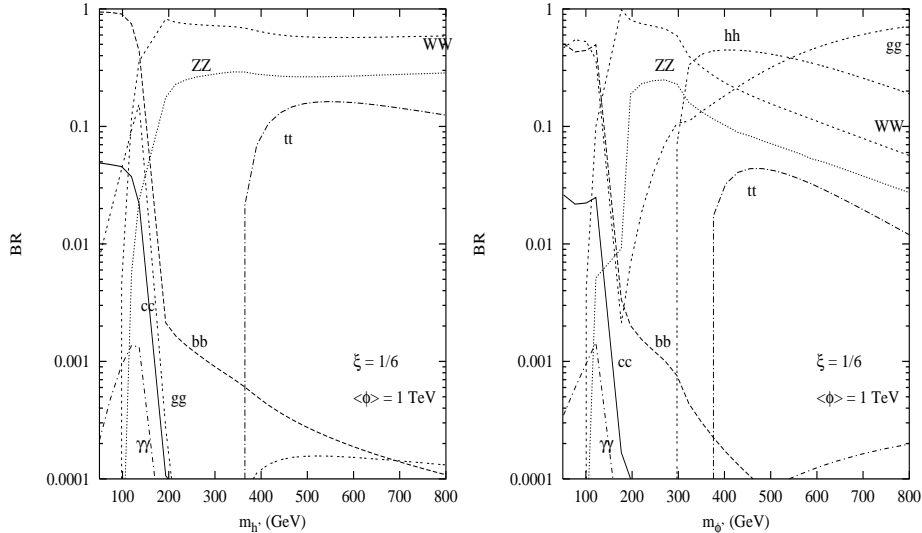


Figure 1: Branching ratios of Higgs and radion decays as functions of  $m_{h'}$  and  $m_{\phi'}$ , respectively. We have used  $\xi = 1/6$ ,  $\Lambda_\phi = 1$  TeV, and  $m_h = 150$  GeV in the plots.

does not bother us as the first term is real, so for the cancellation real part of the second term is more important). For  $\Lambda_\phi = 1$  TeV,  $\xi = 0.167$ , around  $m_{h'} = 250$  GeV, there is a cancellation between these two terms. This drives the  $h'$  width to two gluons to zero around this mass region. We will see that this will also affect the  $h'$  signals. When one changes  $\Lambda_\phi$  to 10 TeV, second term changes very little but the first term is modified (its magnitude is reduced) and thus the cancellation is not so severe in this case. Again when the sign of  $\xi$  is changed, (i.e  $\xi = -0.167$ ) one can easily check that the first term simply changes its sign, while the second term remains almost unchanged. Thus the accidental cancellation between two terms in  $gg$  coupling shows up only in  $\xi > 0$  case. There is no such cancellation in  $\phi'gg$  coupling.

Next we will discuss the production cross-sections of Higgs and radion in gluon-gluon fusion, multiplied by the branching ratios to  $\gamma\gamma$ ,  $ZZ$  and  $WW$  decay modes ( $ZZ$  and  $WW$  cross-sections will be further multiplied by the branching ratios  $Z \rightarrow l^+l^-$  and  $W \rightarrow l\nu_l$ ; where  $l \equiv e, \mu$ ). Gluon-gluon fusion is the dominant production process for the Higgs and production cross-section is further enhanced by the trace anomaly in radion production. In all the figures that we'll present in the following, the c.m. energy of the LHC is assumed to be 14 TeV. We have used  $m_h = 150$  GeV in all our following analysis.

In Figure 2, we show the cross-section of  $pp(gg) \rightarrow \phi'(h') \rightarrow \gamma\gamma$  as a function of  $m_{\phi'}$  ( $m_{h'}$ ). Fig. 2 (a) corresponds to the case  $\xi = 0$ . For the Higgs production the cross-section is same as in the Standard Model. When calculating the proton-proton cross-section from the parton level

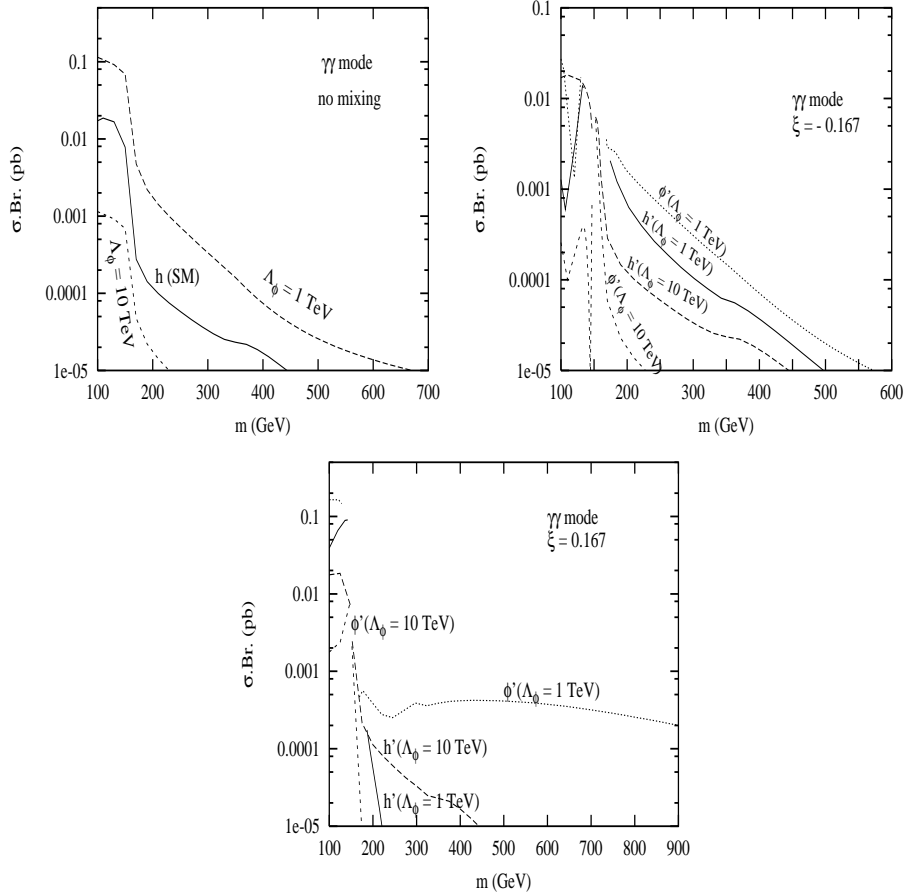


Figure 2: The cross-section of  $pp(gg) \rightarrow \phi'(h') \rightarrow \gamma\gamma$  as a function of  $m_{\phi'}$  ( $m_{h'}$ ) with  $\Lambda_\phi = 1$  TeV and 10 TeV,  $m_h = 150$  GeV, (a)  $\xi = 0$ , (b)  $\xi = -1/6$ , and (c)  $\xi = 1/6$ .

(in this case and in the following), we have used CTEQ4L parton distribution functions [15] with factorization scale set at  $m_{\phi', h'}$ . As seen from the Figure, the radion cross section depends strongly on the radion VEV,  $\Lambda_\phi$ . The cross-section for  $\Lambda_\phi = 1$  TeV is larger than the Higgs cross-section because of the anomaly, extending the detectability of the mode beyond  $m_{\phi'} = 160$  GeV, but the suppression by the radion VEV is evident, when  $\Lambda_\phi = 10$  TeV. In Fig. 2 (b) and (c) we consider the  $\xi \neq 0$  case. Higgs cross-section (in 2(b) and 2(c)) also depends on  $\Lambda_\phi$  because of the mixing. Furthermore, it is clear that the absolute value, as well as the sign of the mixing parameter are crucial for the cross-section. In (b) we set  $\xi = -1/6$ , and in (c)  $\xi = 1/6$ . The Higgs curvature mixing changes the situation dramatically. For the positive mixing, the  $\gamma\gamma$  cross-section is increased for the physical Higgs mass  $m_{h'} < 150$  GeV, while for the negative mixing the cross-section decreases. For  $\xi = 1/6$ , in Fig. 2 (c), if both scalars are lighter than

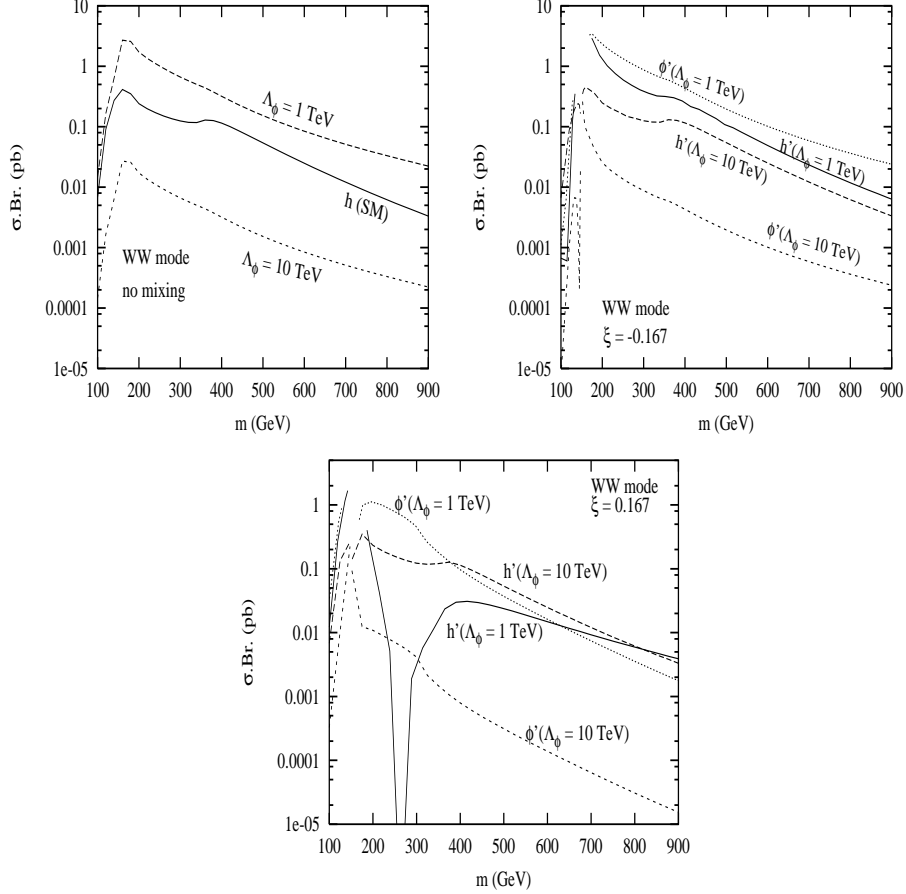


Figure 3: The cross-section of  $pp(gg) \rightarrow \phi'(h') \rightarrow W^+W^- \rightarrow l^+l^-\nu\bar{\nu}$  ( $l \equiv e, \mu$ ) as a function of  $m_{\phi'}$  ( $m_{h'}$ ) with  $\Lambda_\phi = 1$  TeV and 10 TeV,  $m_h = 150$  GeV, (a)  $\xi = 0$ , (b)  $\xi = -1/6$ , and (c)  $\xi = 1/6$ .

$\sim 145$  GeV, they can be detected with enhanced cross-sections if  $\Lambda_\Phi = 1$  TeV. If  $\Lambda_\Phi = 10$  TeV, for a very small range close to 145 GeV two scalars may be detectable. In the case of negative mixing, in Fig. 2 b, the cross-sections for  $\Lambda_\Phi = 1$  TeV are decreased. Two scalars are visible if they are both rather degenerate, with masses around 125 GeV. If  $\Lambda_\Phi = 10$  TeV, one scalar can be detected if it is lighter than 150 GeV. The discontinuities in the scalar masses in the plots are due to the discontinuity in the radion-Higgs mass matrix elements, as seen in the Appendix. We want to point out another gross feature of these plots. For scalar masses less than  $2m_W$ ,  $\gamma\gamma$  cross-section remains almost constant (for no-mixing case) or changes slowly with mass (for  $\xi \neq 0$ ). As soon as the  $2W$  decay mode is open,  $\gamma\gamma$  branching ratio falls off pretty fast for all of the above cases, decreasing the intensity of  $\gamma\gamma$  signal beyond this mass range. The sudden dip and jump of the  $pp \rightarrow \phi' \rightarrow \gamma\gamma, ZZ, WW$  cross-section for  $\Lambda_\Phi = 10$  TeV,  $\xi = -1/6$  around

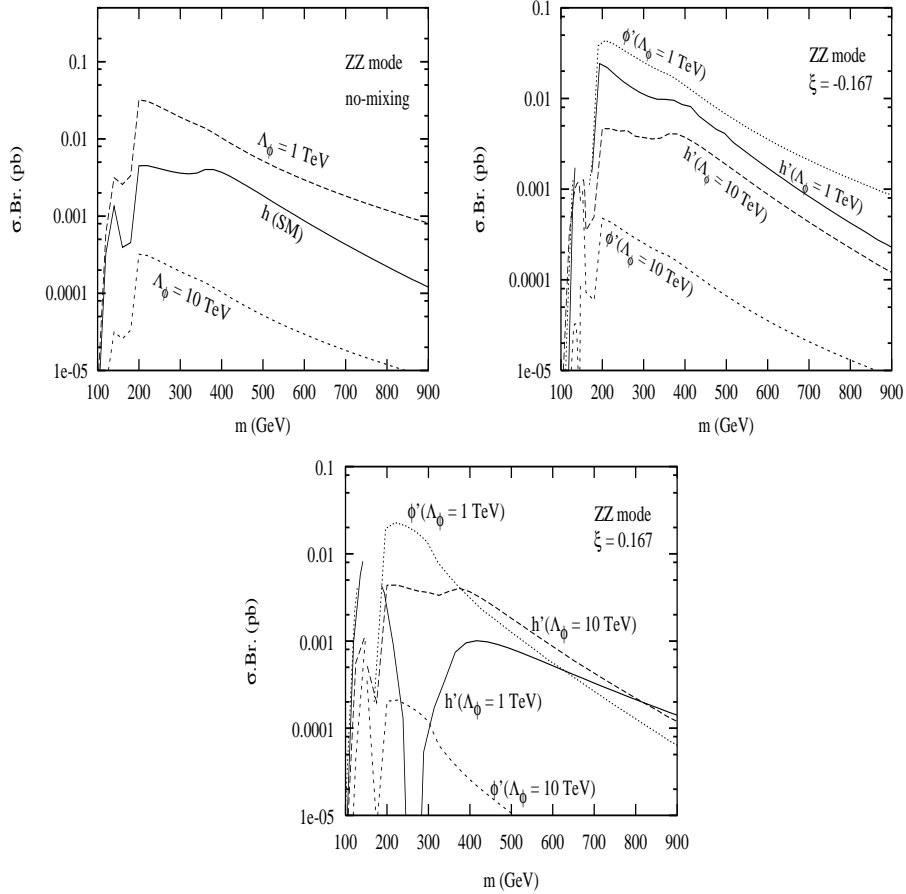


Figure 4: The cross-section of  $pp(gg) \rightarrow \phi'(h') \rightarrow ZZ \rightarrow l^+l^-l^+l^-$  ( $l \equiv e, \mu$ ) as a function of  $m_{\phi'}$  ( $m_{h'}$ ) with  $\Lambda_\phi = 1 \text{ TeV}$  and  $10 \text{ TeV}$ ,  $m_h = 150 \text{ GeV}$ , (a)  $\xi = 0$ , (b)  $\xi = -1/6$ , and (c)  $\xi = 1/6$ .

$m_{\phi'} = 150 \text{ GeV}$  again can be accounted by the variation of  $a_{12}$  in  $\phi'gg$  coupling and also by the choice of the value of the Higgs mass parameter ( $m_h$ ) in our analysis.

In Figure 3 we present the corresponding plots for the process  $pp(gg) \rightarrow \phi'(h') \rightarrow W^+W^- \rightarrow l^+l^-\nu\bar{\nu}$  ( $l \equiv e, \mu$ ), which becomes important in the Standard Model case when the Higgs mass is above approximately  $150 \text{ GeV}$ . In Fig. 3 (a), we set  $\xi = 0$ . While the  $\gamma\gamma$  mode is useful for radion detection up to  $200 \text{ GeV}$  when  $\Lambda_\phi = 1 \text{ TeV}$ , the  $WW$  mode is observable up to around  $400 \text{ GeV}$ . For the  $WW$  mode with  $\Lambda_\phi = 1 \text{ TeV}$  there is a clear increase in the Higgs cross-section, if the mixing parameter is negative, and two scalars should be observable if they are lighter than  $400 \text{ GeV}$ . If  $\Lambda_\phi = 10 \text{ TeV}$ , the Higgs looks similar to the Standard Model Higgs, while radion is unobservable. If the mixing parameter is positive, only one scalar is detectable over most of the mass range, nearly up to  $300 \text{ GeV}$ , for  $\Lambda_\phi = 1 \text{ TeV}$ . Only for light masses, below  $140 \text{ GeV}$ ,



two scalars could be detected. For  $\Lambda_\phi = 10$  TeV, one scalar may be detectable around 200 GeV. Again the sudden dip in the  $WW$  (and also in  $ZZ$ , which we discuss in the following paragraph) production cross-section (via resonance  $h'$  production) around  $m_{h'} = 250$  GeV for  $\Lambda_\phi = 1$  TeV,  $\xi = 1/6$ , can be explained by the vanishing  $h'gg$  coupling around this mass range.

In Figure 4 we plot the cross-section for  $pp(gg) \rightarrow \phi'(h') \rightarrow ZZ \rightarrow l^+l^-l^+l^-$  ( $l \equiv e, \mu$ ), with (a), (b), and (c) corresponding to similar sets of parameters than in the Figures 2 and 3. In the Standard Model this process provides the golden signal of Higgs production, four leptons with no missing energy. The  $H \rightarrow ZZ \rightarrow 4l$  is the best signal for Higgs in the range  $180 \text{ GeV} < m_H < \sim 700 \text{ GeV}$  [14]. For  $\Lambda_\phi = 1$  TeV, there is again obvious increase for the Higgs cross-section if  $\xi = -1/6$ , and the mass range for detecting two scalars increases nearly upto to 800 GeV. For 10 TeV the effects are minor when compared to the Standard Model, except that there are small ranges below 150 GeV, where two scalars can be detected, both for positive and negative mixing parameter.

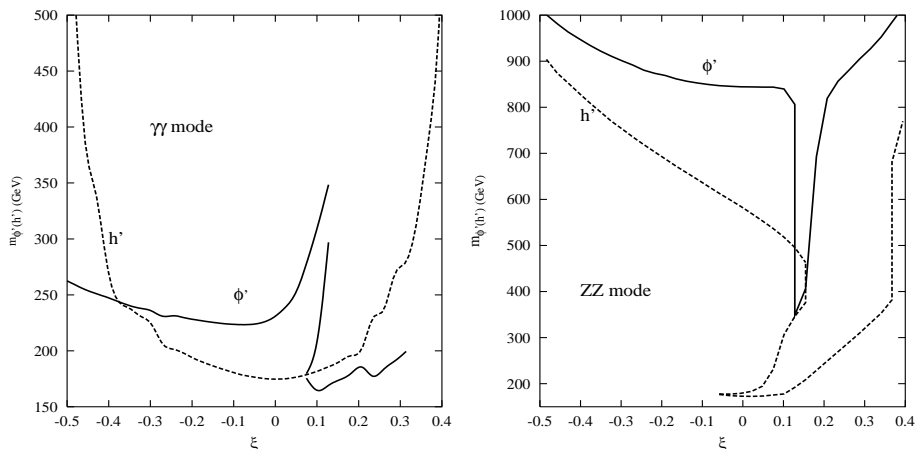


Figure 5: Contours of 100 (a)  $\gamma\gamma$  and (b)  $ZZ$  events from  $\phi'$  (solid line) and  $h'$  (dashed line) production and decay at the LHC in the  $(\xi, m_{h'(\phi)})$  plane. We have assumed  $\Lambda_\phi = 1$  TeV,  $m_h(m_\phi) = 150$  GeV and an integrated luminosity of  $100 \text{ fb}^{-1}$ .

Till now we have considered some specific values of the mixing parameter  $\xi$ . Before we conclude, we discuss how the  $\gamma\gamma$  and  $ZZ$  event rates vary with this parameter. From the consideration of perturbative unitarity,  $|\xi| > 3$  is ruled out [19]. For  $\Lambda_\phi = 1$  TeV,  $\xi$  can vary from  $-0.75$  to  $0.56$ , as one finds from the Appendix A. The role of  $\xi$  is crucial in determining the physical masses of the scalars as well as the couplings of them to the SM fields. The effect of this parameter on the event rates is twofold. In Fig. 5, we have plotted the contours of 100  $\gamma\gamma$  and  $ZZ$  ( $l^+l^-l^+l^-$ ) events from  $\phi'$  and  $h'$  production and decay at the LHC in  $(\xi, m_{h'(\phi)})$  -plane.

For this calculation we have assumed  $\Lambda_\phi = 1 \text{ TeV}$ ,  $m_h (m_\phi) = 150 \text{ GeV}$  and an integrated luminosity of  $100 \text{ fb}^{-1}$ .

Sudden jumps in the event contours around specific values of  $\xi$  are due to the discontinuities in the physical masses and sharp maxima/minima of the relevant couplings, which we have pointed out earlier. Especially, at around  $\xi \sim 0.3$ , the  $\phi' - \gamma - \gamma$  coupling strongly reduces making the corresponding mass reach too low to be shown in the Figure 5. Apart from these irregularities, both  $\phi'$  and  $h'$  event rates significantly increase with the absolute value of the mixing parameter for the  $ZZ \rightarrow l^+l^-l^+l^-$  channel, and  $h'$  rates for the  $\gamma\gamma$  channel. The  $h'$  event rate is more sensitive to the mixing parameter which is evident from both the channels. We have checked that physical masses are nearly symmetric with respect to the positive and negative values of  $\xi$ . The  $h'$  event rate via  $\gamma\gamma$  channel is almost symmetric in positive and negative values of  $\xi$ . Almost for all negative values of  $\xi$ , mass reach for  $\phi' \rightarrow \gamma\gamma$  channel is better than for  $h' \rightarrow \gamma\gamma$  channel. In the  $ZZ$  channel, almost for any  $\xi$ , the mass reach is better for  $\phi'$ , and the  $\phi'$  event rate is symmetric about  $\xi = 0$  apart from one sharp dip around  $\xi \simeq 0.1$ . This is due to the sudden dip in the  $\phi' - g - g$  coupling. We have not presented the corresponding plots for the  $WW$  channels. Production mechanism for both the  $WW$  and  $ZZ$  channels are the same. The  $\phi', h' \rightarrow WW \rightarrow l^+\nu l^-\bar{\nu}$  effective branching ratio is almost an order of magnitude greater than that of  $\phi', h' \rightarrow ZZ \rightarrow l^+l^-l^+l^-$  channel. Therefore, it is evident that the mass reach of the  $WW$  channel is better than that of the  $ZZ$  channel for a particular value of  $\xi$ . The dependence of the mass reach on  $\xi$  for the  $WW$  channel is the same as for the  $ZZ$  channel.

#### IV. Conclusion

We have studied the Higgs and radion production via gluon-gluon fusion in the RS model with curvature-Higgs mixing. Our results show that radion and Higgs production from  $gg$  collision will be very different in mixed and unmixed cases. Thus the detection of Higgs or radion at the LHC may reveal the mixing strength, including sign, in the model.

The decay modes of radion and Higgs in the mixing case will be quite different from unmixed case. Especially, the abnormal coupling of radion to gauge bosons can effect Higgs decay through mixing, thus modifying the Higgs decay strongly. When two Higgs like scalars are seen, the different decay branching ratios, when compared to the minimal supersymmetric standard model (MSSM), will help to distinguish between MSSM and the RS model.

#### Acknowledgement

The authors thank the Academy of Finland (project number 163394 and 48787) for financial support. Z.-H. Yu thanks the World Laboratory, Lausanne, for the scholarship. A. Datta

acknowledges the hospitality of Helsinki Institute of Physics where this work has been done.

## Appendix

### A. The curvature-Higgs mixing:

After shifting  $\phi \rightarrow \phi + \Lambda_\phi$  in Eqn. (2.1), the Lagrangian containing bilinear terms of radion and Higgs is obtained as

$$\mathcal{L} = -\frac{1}{2}\phi[(1 - 6\xi\gamma^2)\square + m_\phi^2]\phi - \frac{1}{2}h(\square + m_h^2)h - \frac{6\xi v}{\Lambda_\phi}\phi\square h. \quad (\text{A.1})$$

Here  $m_\phi$  is a mass parameter for  $\phi$ .

After diagonalisation, the fields should be redefined as

$$\phi = a\phi' + bh', \quad (\text{A.2})$$

$$h = c\phi' + dh', \quad (\text{A.3})$$

where  $a = \cos\theta/Z$ ;  $b = -\sin\theta/Z$ ;  $c = \sin\theta - 6\xi\gamma/Z \cos\theta$  and  $d = \cos\theta + 6\xi\gamma/Z \sin\theta$ , with  $Z^2 = 1 - 6\xi\gamma^2(1 + 6\xi)$  and the mixing angle  $\theta$  is given by

$$\tan 2\theta = 12\xi\gamma Z \frac{m_h^2}{m_h^2(Z^2 - 36\xi^2\gamma^2) - m_\phi^2}. \quad (\text{A.4})$$

Our results agree with those in Ref. [11] (with  $\xi\gamma \ll 1$ ) and in Ref. [12]. From Eq. (A.3-4), we see clearly the constraints  $-(1 + \sqrt{1 + 4/\gamma^2})/12 \leq \xi \leq (\sqrt{1 + 4/\gamma^2} - 1)/12$ , just as in Ref. [12].

The new fields  $\phi'$  and  $h'$  are mass eigenstates with masses

$$m_{\phi'}^2 = c^2 m_h^2 + a^2 m_\phi^2, \quad (\text{A.5})$$

$$m_{h'}^2 = d^2 m_h^2 + b^2 m_\phi^2. \quad (\text{A.6})$$

The interaction Lagrangian of  $\phi$  and  $h$  with fermions and massive gauge bosons,

$$\mathcal{L} = -\frac{1}{v}(m_{ij}\bar{\psi}_i\psi_j - M_V^2 V_{A\mu}V_A^\mu) \left[ h + \frac{v}{\Lambda_\phi}\phi \right], \quad (\text{A.7})$$

can be transformed to the coupling of mass eigenstates  $\phi'$  and  $h'$  to fermions and massive gauge bosons as

$$\mathcal{L} = -\frac{1}{\Lambda_\phi}(m_{ij}\bar{\psi}_i\psi_j - M_V^2 V_{A\mu}V_A^\mu) \left[ a_{34} \frac{\Lambda_\phi}{v} h' + a_{12} \phi' \right], \quad (\text{A.8})$$

where  $a_{12} = a + c/\gamma$  and  $a_{34} = d + b\gamma$ . The coefficients  $a_{12}$  and  $a_{34}$  give directly the strength of the corresponding interaction when compared to the case with no mixing.

## B. Form factors

The form factors  $F_{1/2}(\tau_t)$  and  $F_1(\tau_W)$  can be defined as [11, 18]

$$F_{1/2}(\tau) = -2\tau[1 + (1 - \tau)f(\tau)] \quad (B.1)$$

and

$$F_1(\tau) = 2 + 3\tau + 3\tau(2 - \tau)f(\tau), \quad (B.2)$$

where  $\tau_t = 4m_t^2/q^2$ ,  $\tau_W = 4m_W^2/q^2$  and

$$f(\tau) = \begin{cases} [\sin^{-1}(1/\sqrt{\tau})]^2, & \tau \geq 1, \\ -1/4[\text{Log}(\eta_+/\eta_-) - i\pi]^2, & \tau < 1, \end{cases} \quad (B.3)$$

with  $\eta_{\pm} = 1 \pm \sqrt{1 - \tau}$ .

## References

- [1] N. Arkani-Hamed, S. Dimopoulos and G. Dvali, Phys. Lett. **B429** (1998) 263; N. Arkani-Hamed, S. Dimopoulos and G. Dvali, Phys. Lett. **B436** (1998) 257.
- [2] L. Randall and R. Sundrum, Phys. Rev. Lett. **83** (1999) 3370; L. Randall and R. Sundrum, Phys. Rev. Lett. **83** (1999) 4690.
- [3] W.D. Goldberger and M.B. Wise, Phys. Rev. Lett. **83** (1999) 4922; W.D. Goldberger and M.B. Wise, Phys. Rev. **D60** (1999) 107505.
- [4] M. Luty and R. Sundrum, Phys. Rev. **D62** (2000) 035008.
- [5] C. Csaki, M. Graesser, L. Randall and J. Terning, Phys. Rev. **D62** (2000) 045015.
- [6] W.D. Goldberger and M.B. Wise, Phys. Lett. **B475** (2000) 275.
- [7] U. Mahanta and S. Rakshit, Phys. Lett. **B480** (2000) 176; U. Mahanta and A. Datta, Phys. Lett. **B483** (2000) 196.
- [8] S. Bae, P. Ko, H.S. Lee and J. Lee, Phys. Lett. **B487** (2000) 299; S. Bae, and H.S. Lee, hep-ph/0011275.
- [9] K. Cheung, Phys.Rev.**D** 63 (2001) 056007, hep-ph/0009232; S.R. Choudhury, A.S. Cornell and G.C. Joshi, hep-ph/0012043.

- [10] S.C. Park, H.S. Song and J. Song, hep-ph/0103308.
- [11] G.F. Giudice, R. Rattazzi and J.D. Wells, Nucl. Phys. **B 595** (2001) 250.
- [12] C.Csaki, M. Graesser and G. Kribs, Phys. Rev. **D63** (2001) 065002.
- [13] M. Chaichian, K. Huitu, A. Kobakhidze and Z.-H. Yu, Phys. Lett.**B** 515 (2001) 65.
- [14] ATLAS Detector and Physics Performance: Technical Design Report, 1, CERN-LHCC-99-014, 1999.
- [15] H. Lai et al., Phys. Rev. **D55** (1997) 1297.
- [16] G. Dvali, G. Gabadadze and M. Porrati, Phys. Lett. **B485** (2000) 208; H. Collins and B. Holdom, Phys. Rev. **D62** (2000) 124008.
- [17] R. Crewther, Phys. Rev. Lett. **28** (1972) 1421; M. Chanowitz and J. Ellis, Phys. Lett. **40B** (1972) 397; K.R. Dienes, E. Dudas and T. Gherghetta, Nucl. Phys. **B567** (2000) 111.
- [18] J.F. Gunion, H.E. Haber, G.L. Kane and S. Dawson, *The Higgs Hunter's Guide*, Addison-Wesley: Redwood City, California, 1989.
- [19] T. Han, G. D. Kribs, and B. McElrath, Phys. Rev. **D64** (2001) 076003.